RSC Advances

PAPER

View Article Online
View Journal | View Issue

Cite this: *RSC Adv.*, 2019, **9**, 39536

Design and synthesis of hierarchical NiO/$Ni_3V_2O_8$ nanoplatelet arrays with enhanced lithium storage properties†

Yang Li,* Feng Duan, Shuai Yang, Qihuang Deng, Songli Liu and Cheng Peng

Hierarchical NiO/$Ni_3V_2O_8$ nanoplatelet arrays (NPAs) grown on Ti foil were prepared as free-standing anodes for Li-ion batteries (LIBs) *via* a simple one-step hydrothermal approach followed by thermal treatment to enhance Li storage performance. Compared to the bare NiO, the fabricated NiO/$Ni_3V_2O_8$ NPAs exhibited significantly enhanced electrochemical performances with superior discharge capacity (1169.3 mA h g^{-1} at 200 mA g^{-1}), excellent cycling stability (570.1 mA h g^{-1} after 600 cycles at current density of 1000 mA g^{-1}) and remarkable rate capability (427.5 mA h g^{-1} even at rate of 8000 mA g^{-1}). The excellent electrochemical performances of the NiO/$Ni_3V_2O_8$ NPAs were mainly attributed to their unique composition and hierarchical structural features, which not only could offer fast Li^+ diffusion, high surface area and good electrolyte penetration, but also could withstand the volume change. The *ex situ* XRD analysis revealed that the charge/discharge mechanism of the NiO/$Ni_3V_2O_8$ NPAs included conversion and intercalation reaction. Such NiO/$Ni_3V_2O_8$ NPAs manifest great potential as anode materials for LIBs with the advantages of a facile, low-cost approach and outstanding electrochemical performances.

Received 10th October 2019
Accepted 25th November 2019

DOI: 10.1039/c9ra08252b

rsc.li/rsc-advances

1 Introduction

Li-ion batteries (LIBs) have attracted much interest as electrochemical energy storage devices due to their outstanding performances in terms of high energy density, high voltage, long lifespan and environmental benignity.[1–3] However, conventional graphite anodes have a low theoretical capacity (372 mA h g^{-1}), which hardly meets the growing energy demand for various consumer electronic devices. In the past few decades, extensive research has been devoted to develop alternative electrode materials aiming for higher energy/power density, longer cycle life, increased safety and lower cost. Nowadays, transition metal oxides (TMOs) exhibit great specific capacities, high volumetric energy densities and intrinsically enhanced safety, making them the supposed alternative anode materials for LIBs.[4–8]

Nickel oxide (NiO) was one of the distinguished candidates, which was not only easy to synthesize, but also had high theoretical capacity (718 mA h g^{-1}) with great chemical/thermal stability.[9,10] However, its low electronic/ionic conductivity and structure destruction in cycling hindered the application of NiO anodes in LIBs. One attractive strategy toward assuaging these problems is to build various nanostructured electrode materials, such as nanoparticles,[11,12] nanospheres,[13] nanorodes[14] and nanosheets.[15,16] Nanostructured electrodes materials can alleviate the stress-induced structural variation derived from repeated lithiation/delithiation process, and provide short diffusion path for electron/ion transfer compared with their bulk counterparts.[17–20] Remarkably, the electrode materials aligned directly on current collectors with hierarchical nanostructure exhibit outstanding electrochemical activities, due to the potential for providing a larger surface area to improve the interfacial kinetics, more space to buffer the volume variation and easier pathways for electrolyte penetration.[21–23]

Another effective approach is to rely largely on designing different ternary transition metal oxides by introducing various metal species into target products, which can synergistically enhance electrochemical properties owning to their enhanced electrochemical activities, electrical conductivity and mechanical stability.[24,25] The nickel-based ternary transition metal oxides, such as $NiCo_2O_4$,[26] $NiMn_2O_4$ (ref. 27) and $NiMoO_4$ (ref. 28) have been examined as potential anode materials for LIBs. Among them, $Ni_3V_2O_8$ has a wide range of energy storage applications.[29,30] For example, ordered mesoporous carbon supported $Ni_3V_2O_8$ composites,[31] $Ni_3V_2O_8$ amorphous wire encapsulated in crystalline tube nanostructure,[32] $Ni_3V_2O_8$/carbon cloth hierarchical structures[33] showed great storage capacities, holding great promise in LIBs.

Recently, various hybridizing metal oxides with an integrate nanostructure have attracted much attention in exploring

College of Materials Science and Engineering, Yangtze Normal University, Chongqing, 408100, People's Republic of China. E-mail: yangli_yznu@163.com; Fax: +86-23-72790029; Tel: +86-23-72790029

† Electronic supplementary information (ESI) available. See DOI: 10.1039/c9ra08252b

alternative anode materials for LIBs as they can take advantage of interaction of different components for enhanced electrochemical performances.[34–39] For instance, Lou *et al.*[40] successfully synthesized a novel Co_3O_4@$Co_3V_2O_8$ hollow structure with a metal organic framework, which exhibited superior electrochemical activity. Bases on the appealing concept, many NiO-based nanocomposites, such as NiO–Co_3O_4 nanoplate,[41] porous NiO–ZnO hybrid nanofibers[42] and hierarchical porous NiO–$NiMoO_4$ heterostructure[43] have been fabricated and tested as high-performance anode materials for LIBs. Only very recently, P. Vishnukumar *et al.*[44] successfully synthesized NiO/$Ni_3V_2O_8$ nanocomposite by a solvothermal method, which exhibited outstanding super-capacitive activity. However, its application for LIBs is rarely reported until now. Furthermore, there is no research on the direct growth of NiO/$Ni_3V_2O_8$ hierarchical nanostructures on conductive collectors for superior lithium storage properties.

In this study, we described a facile one-step hydrothermal approach to fabricate a hierarchical NiO/$Ni_3V_2O_8$ nanoplatelet arrays (NPAs) directly grown on Ti foil, followed by thermal treatment. In this architecture, the interpenetrated NiO/$Ni_3V_2O_8$ nanoplatelets assembled into a framework, in which the NiO and $Ni_3V_2O_8$ were homogeneously dispersed at the nanoscale. The newly synthesized NiO/$Ni_3V_2O_8$ NPAs benefited from novel *in situ* electrochemical reconstruction exhibited high specific capacity, excellent cycling stability and great storage capability. The mechanism of lithiation/delithiation of new NiO/$Ni_3V_2O_8$ NPAs was also explored *via ex situ* XRD measurements, making contributions to the application of transition metal oxides for energy storage.

2 Experimental sections

2.1 Synthesis of NiO/$Ni_3V_2O_8$ NPAs

All the reagents, HCl (3 M), ethanol, acetone and deionized water, used in the study were of analytical grade to eliminate impurities on the surface of Ti foil. In a typical synthesis, 1 mmol Na_3VO_4 and 1 mmol $NiCl_2 \cdot 6H_2O$ were dissolved into 80 mL deionized water with vigorous magnetic stirring. Subsequently, 7 mmol $NiCl_2 \cdot 6H_2O$ and 50 mmol $CO(NH_2)_2$ were dissolved in another fresh 80 mL distilled water followed by adding above solution under stirring. The mixed solution was continuous stirring for 15 min and then transferred into a 200 mL Teflon-lined autoclave with inserting a piece of clean Ti foil and maintained at 160 °C for 8 h. The resultant substrate was fetched out and washed with distilled water several times, then dried in oven at 60 °C and annealed at 400 °C in the air for 3 h to obtain the NiO/$Ni_3V_2O_8$ NPAs. As a comparison, the bare NiO samples were also prepared under the same condition without the addition of Na_3VO_4 in precursor solution. The integrated synthesis process for the NiO/$Ni_3V_2O_8$ NPAs was depicted in Fig. 1.

2.2 Materials characterization

The crystal phase of the product was characterized by X-ray diffraction patterns (XRD, Rigaku D/MAX 2400). The morphology and microstructure of the specimen was characterized by Scanning Electron Microscope (SEM, JEOL, JSM-6701F) and Transmission Electron Microscope (TEM, JEOL, JEM-2010) with Energy Dispersive Spectrometer (EDS). The composition of the sample was analyzed by Inductively Coupled Plasma (ICP-AES, IRIS Intrepid II XSP).

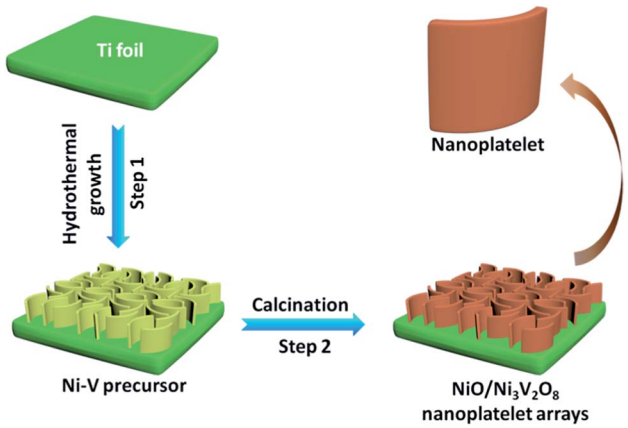

Fig. 1 Illustration of NiO/$Ni_3V_2O_8$ NPAs formation process.

2.3 Electrochemical measurements

The electrochemical performance was measured by CR2032 coin cells assembled with the NiO/$Ni_3V_2O_8$ as working electrode, Li foil, Celgard 2300 membrane and electrolyte in a mixture of 1 M $LiPF_6$ in ethylene carbonate (EC) and dimethyl carbonate (DMC) (1 : 1, by volume). The mass loading of the active materials was around 1–1.3 mg cm^{-2}. Cyclic voltammetry (CV) was carried out on an electrochemical workstation (CHI660E). The galvanostatic charging–discharging test was performed on the Li-ion battery cycler (LAND CT2001A) at different current rates. The electrochemical impedance spectroscopy (EIS) was measured on an electrochemical workstation (CHI660E).

3 Results and discussion

3.1 Synthesis and characterization

Fig. 2a showed the XRD pattern of NiO/$Ni_3V_2O_8$ NPAs. The diffraction peaks were located at 37.2, 43.2, 62.8 and 74.4 degree ascribing to the (101), (012), (110) and (113) faces of NiO (JCPDF card no. 44-1159), whereas the diffraction peaks were located at 15.5, 29.9, 35.9 and 64.0 degree originating from the phase of $Ni_3V_2O_8$ (JCPDF card no. 74-1484). There were no other detectable phases. Furthermore, the results of EDS (Fig. 2b) confirmed that the specimen was only constituted with NiO and $Ni_3V_2O_8$. The Ni/V atomic ratio determined by ICP technique of two specimens was about 7.58 : 1 (Table S1†), corresponding to 30.8% (mass percentage) of $Ni_3V_2O_8$ in NiO/$Ni_3V_2O_8$ NPAs.

The morphology and microstructure of the as-fabricated NiO/$Ni_3V_2O_8$ NPAs on Ti foil were characterized by SEM and TEM. Fig. 3a and b showed that the NiO/$Ni_3V_2O_8$ NPAs had an

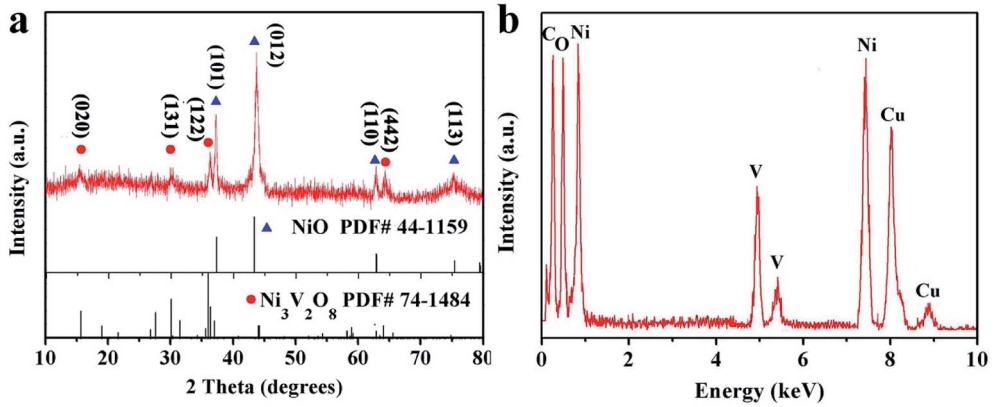

Fig. 2 (a) XRD and (b) EDS pattern of $NiO/Ni_3V_2O_8$ NPAs.

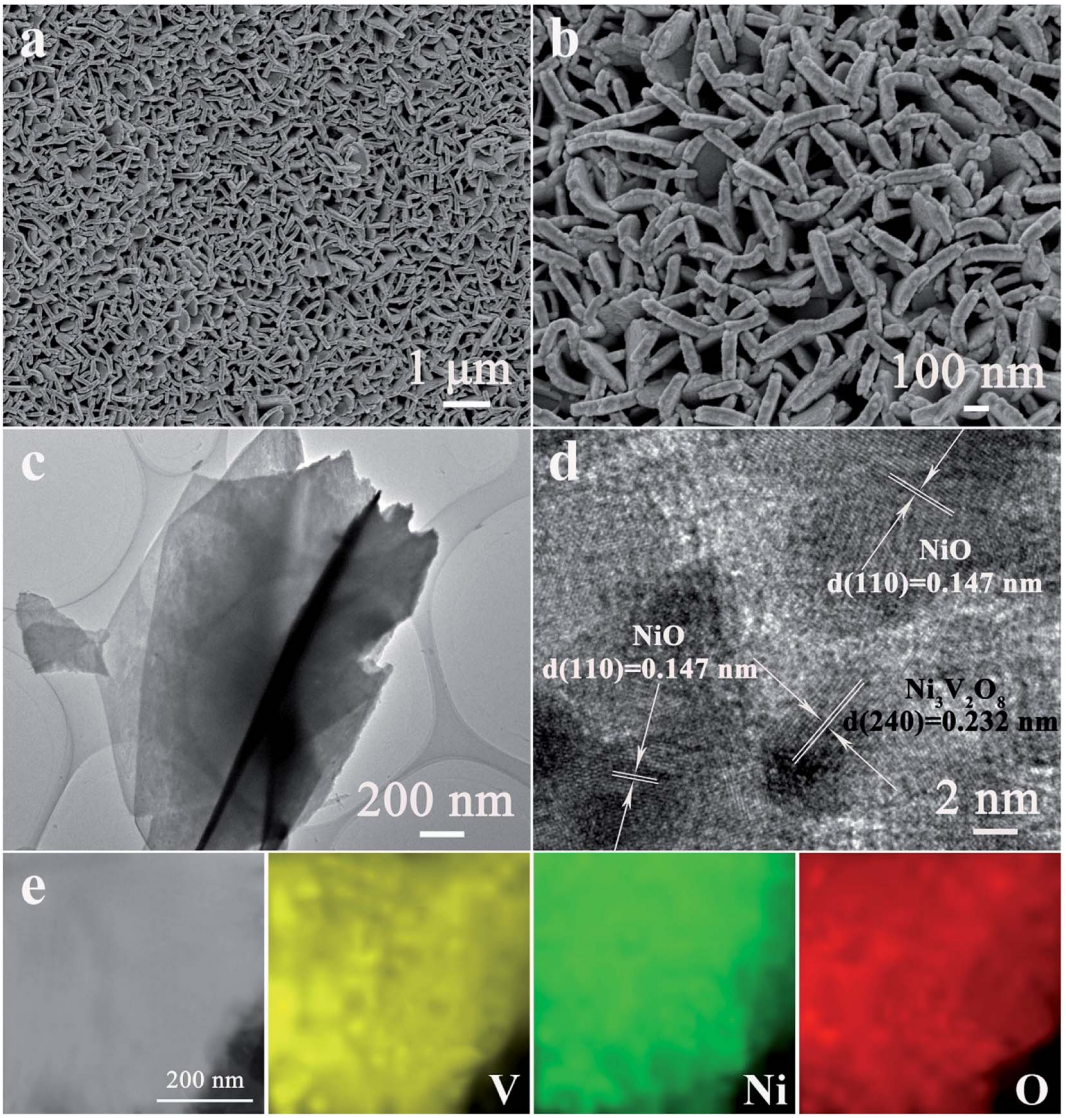

Fig. 3 (a and b) SEM and (c) TEM images of $NiO/Ni_3V_2O_8$ NPAs. (d) High resolution TEM image of $NiO/Ni_3V_2O_8$ NPAs. (e) The scan TEM image and the corresponding EDS elemental mapping images of Ni, V, and O.

open and highly porous framework structure assembled by interpenetrated nanoplatelets, homogeneously anchored on the surface of Ti foil. In contrast, the NiO samples displayed a bulk structure with size of around several microns as shown in Fig. S1.† The TEM image (Fig. 3c) further verified the nanoplatelet structure of NiO/$Ni_3V_2O_8$ NPAs, which was consistent with SEM result obtained from Fig. 3b. The thickness of a single NiO/$Ni_3V_2O_8$ nanoplatelet was estimated to be about 60–80 nm. The high-resolution TEM image of NiO/$Ni_3V_2O_8$ NPAs (Fig. 3d) showed that the lattice spacings were 0.147 and 0.232 nm for the (110) crystal planes of NiO, and (240) crystal planes of $Ni_3V_2O_8$, respectively. The corresponding selected-area electron diffraction (SEAD) pattern showed that the NiO/$Ni_3V_2O_8$ NPAs were well crystallized and polycrystalline (Fig. S2†). The scan TEM image and the EDS mappings of NiO/$Ni_3V_2O_8$ NPAs (Fig. 3e) revealed the uniform distribution of Ni, V and O elements. This result confirmed that the NiO and $Ni_3V_2O_8$ subunits were homogeneously dispersed in the NiO/$Ni_3V_2O_8$ NPAs and contacted with each other intimately.

3.2 Electrochemical performances of the electrodes

The electrochemical performance of NiO/$Ni_3V_2O_8$ NPAs was tested as an anode for LIBs. Fig. 4a showed CV cures of NiO/$Ni_3V_2O_8$ NPAs ranged from 0.01 to 3.0 V (*vs.* Li/Li^+) with 0.1 mV s^{-1} scan rate. During the first discharge cycle, a broad reduction peak was observed at around 1.38 V, which might result from the reduction of $Ni_3V_2O_8$ into NiO companied with the formation of $Li_xV_2O_5$.[45] The broad irreversible cathodic peak was located at 0.75–0.01 V corresponding to the reduction of NiO to Ni, the insertion of Li^+ into $Li_xV_2O_5$ and the formation of solid electrolyte interface (SEI).[31] The reduction peaks shifted to 1.89 V, 1.03 V and 0.72 V in the subsequent cycles, which could be attributed to the possible activation process as described by Sambandam *et al.*,[46] including the phase transformation, structural reorganization and a polarization change in the sample material. During the first charging cycle, the oxidation peak was observed at around 1.25 V, corresponded to the oxidation of Ni into NiO, and two weak reduction peaks was located at 2.0–3.0 V attributing to the extraction of Li^+ from $Li_xV_2O_5$. In addition, the overlapped CV curves from the second

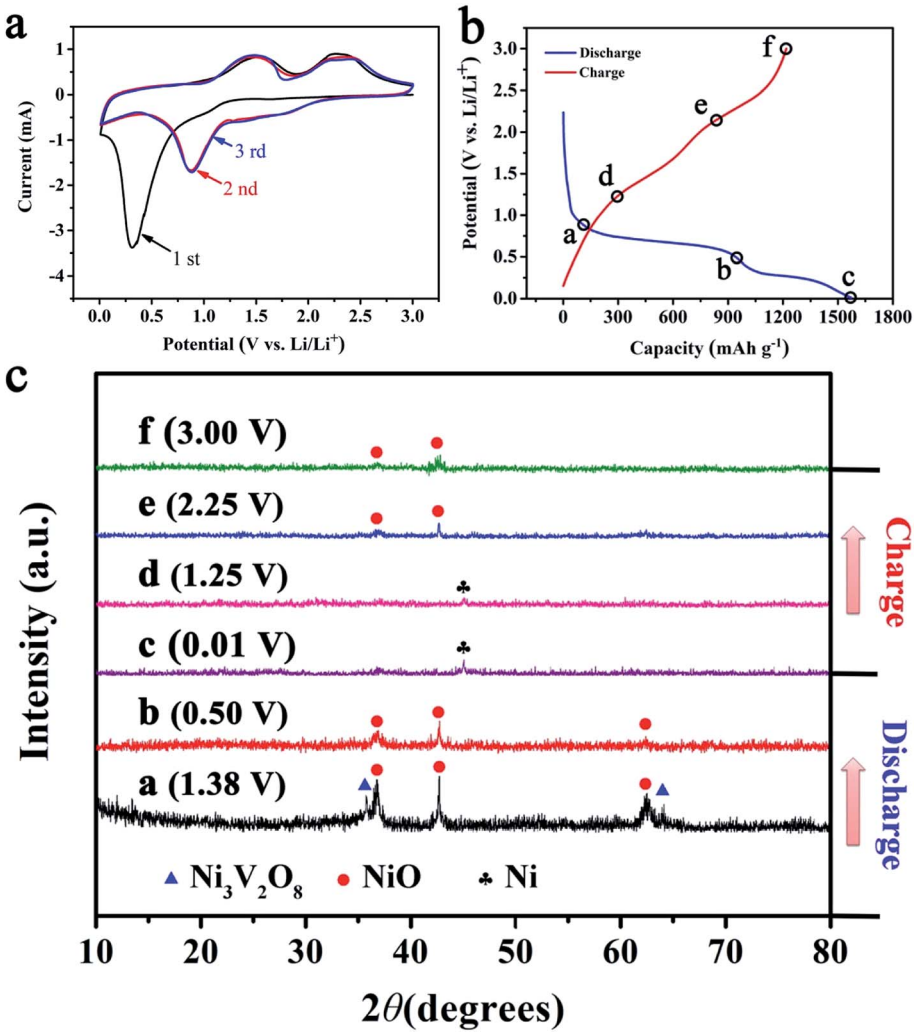

Fig. 4 (a) The CV curves of NiO/$Ni_3V_2O_8$ nanohybrides for the first three cycles. (b and c) The *ex situ* XRD patterns of NiO/$Ni_3V_2O_8$ nanohybrides under different discharge and charge states.

cycle onward indicated a good stability and cyclability for the insertion and extraction of Li^+.

In order to investigate the mechanism of lithiation/delithiation of $NiO/Ni_3V_2O_8$ NPAs, a series of partially lithiated $NiO/Ni_3V_2O_8$ NPAs with various charge and discharge states (denoted with letters "a" to "f" in Fig. 4b and c) during the first cycle were examined by the *ex situ* X-ray (Fig. 4c). Fig. 4c-a demonstrated that the $Ni_3V_2O_8$ phase gradually turned to the NiO phase (JCPDF card no. 44-1159) and amorphous $Li_xV_2O_5$ with discharging from 3.00 V to 1.38 V. Then, the intensity of NiO at the peak reduced sharply, and the diffraction peaks of $Ni_3V_2O_8$ disappeared when discharging to 0.50 V (Fig. 4c-b), implying the conversion reaction of NiO to Ni accompanied with the reduction of all the $Ni_3V_2O_8$ into NiO and $Li_xV_2O_5$. After discharging to 0.01 V (Fig. 4c-c), the peak of NiO disappeared and a new phase of Ni (JCPDF card no. 03-1051) appeared, which corresponded to a conversion reaction of NiO to Ni and the insertion of Li^+ into $Li_xV_2O_5$. Finally, the peak of Ni

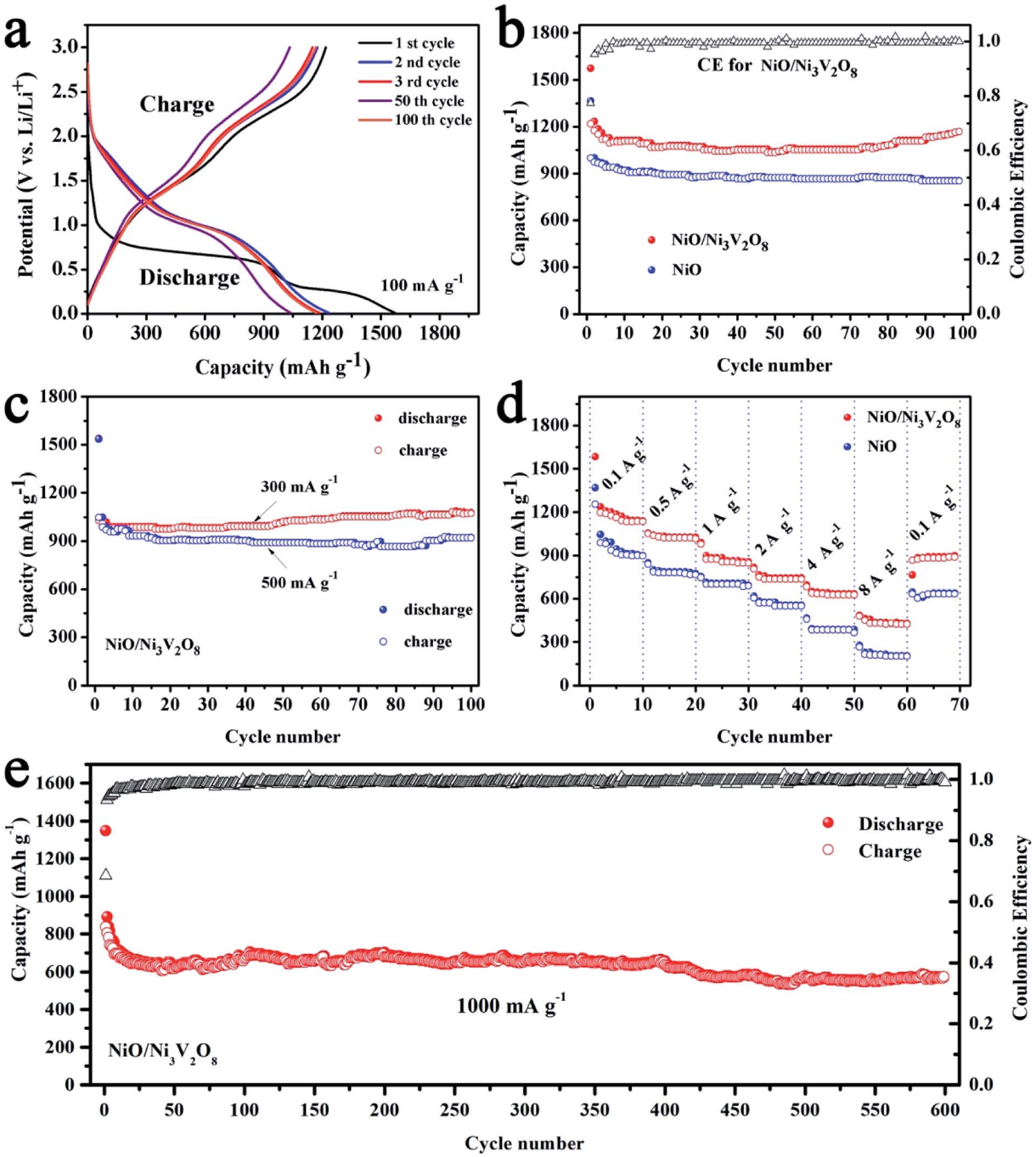

Fig. 5 (a) The charge–discharge profiles of $NiO/Ni_3V_2O_8$ NPAs. (b) Comparison of cycling performance of $NiO/Ni_3V_2O_8$ NPAs and NiO samples. (c) The cycling performance of $NiO/Ni_3V_2O_8$ NPAs at 300 and 500 mA g^{-1}. (d) Rate capability testing at various current densities. (e) Long cycling performance of the $NiO/Ni_3V_2O_8$ NPAs at a large specific current of 1000 mA g^{-1}.

gradually disappeared and the NiO phase reappeared with increased charging degree (Fig. 4c-d and f), which could attribute to the oxidation of Ni into NiO and the extraction of Li^+ from $Li_xV_2O_5$.

As discussed above, the electrochemical mechanism of NiO/$Ni_3V_2O_8$ NPAs based on conversion and intercalation reaction could be represented as follows:

$$NiO + Ni_3V_2O_8 + xLi^+ + xe^- \rightarrow 4NiO + Li_xV_2O_5 \quad (1)$$

$$NiO + 2Li^+ + 2e^- \leftrightarrow NiO + Li_2O \quad (2)$$

$$Li_xV_2O_5 + yLi^+ + ye^- \leftrightarrow Li_{x+y}V_2O_5 \quad (3)$$

The discharge–charge cycling test were carried out at 100 mA g^{-1} with the voltage window of 0.01–3 V to assess the cycle performance of the NiO/$Ni_3V_2O_8$ NPAs (Fig. 5a). Results showed that there were two discharge potential plateaus located at 1.75 V and 0.25 V during the first discharge process. The initial discharge and charge capacities were 1572.4 and 1366.2 mA h g^{-1}, respectively, corresponding to an irreversible capacity of 13.1%. The large capacities loss was common for metal-oxide based anodes due to the formation of SEI film caused by electrolyte degradation.[47,48] Meanwhile, the capacity of the NiO/$Ni_3V_2O_8$ NPAs in the 100th cycle was similar to the 3rd cycle and higher than that of 50th cycle, representing the good stability of the NiO/$Ni_3V_2O_8$ NPAs. It is interesting that the specific capacities of the NiO/$Ni_3V_2O_8$ NPAs decreased slowly in initial 50 cycles, and then increased gradually, finally reached up to 1169.3 mA h g^{-1} after 100 cycles as demonstrated in the cycling performance for NiO/$Ni_3V_2O_8$ NPAs at 100 mA g^{-1} (Fig. 5b). The increasing capacity might originate from gradual participation in electrochemical reaction of active NiO/$Ni_3V_2O_8$ NPAs along with cycling number.[49] The coulombic efficiency (CE) of initial cycle for NiO/$Ni_3V_2O_8$ NPAs was 86.9%. After that, the values of CE increased significantly, and then kept stable in subsequent cycles, suggesting good capacity recovery ability. Fig. 5c showed that the initial discharge capacities were 1538.3 and 1535.1 mA h g^{-1} at current of 300 and 500 mA g^{-1}, and retained at 1076.5 and 922.1 mA h g^{-1}, after 100 cycles, respectively. As a comparison, the bare NiO samples only delivered a low capacity of 852.8 mA h g^{-1} after 100 cycles at the current density of 100 mA g^{-1}. In summary, the as-prepared NiO/$Ni_3V_2O_8$ NPAs showed distinct enhancement over the reported NiO-based and $Ni_3V_2O_8$-based anodes as summarized in Table S2.†[32,37,41,42,50,51]

Results from the rate performance of the NiO/$Ni_3V_2O_8$ NPAs (Fig. 5d) showed that the discharge capacities of NiO/$Ni_3V_2O_8$ NPAs were 1138.4, 1026.9, 857.5, 744.4 and 634.2 mA h g^{-1} at the current densities of 100, 500, 1000, 2000 and 4000 mA g^{-1}, respectively. Even at a high rate of 8000 mA g^{-1}, a large capacity of 427.5 mA h g^{-1} was still obtained, which was higher than the theoretical capacity of commercial graphite (372 mA h g^{-1}). In

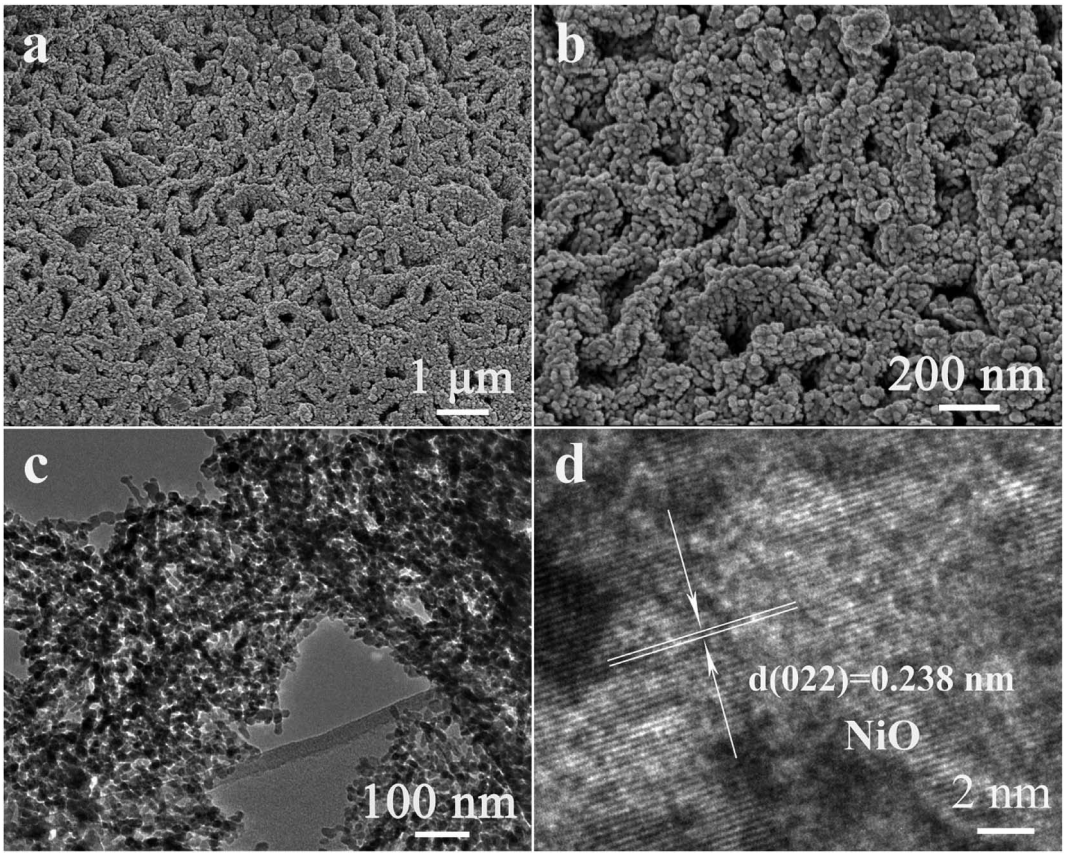

Fig. 6 (a) The SEM, (b) TEM, (c) SEAD and (d) HRTEM images of NiO/$Ni_3V_2O_8$ NPAs after 100 cycles with different magnification.

addition, upon altering the current density back to 100 mA g^{-1} after high rate discharge–charge cycling, a capacity of 898.3 mA h g^{-1} could be recovered, indicating the great rate performance of $NiO/Ni_3V_2O_8$ NPAs. In contrast, the capacities of NiO samples were much lower than these of $NiO/Ni_3V_2O_8$ NPAs under the same tested conditions. The superior rate performance of the $NiO/Ni_3V_2O_8$ NPAs could be closely related to their superior conductivity. In addition, $NiO/Ni_3V_2O_8$ NPAs performance was exceptional for long cycling at a high current density of 1000 mA g^{-1}. Fig. 5e showed that the reversible discharge capacity reached 570.1 mA h g^{-1} after 600 cycles. The CE of the $NiO/Ni_3V_2O_8$ NPAs was as high as 99.9% within 600 cycles, demonstrating highly reversible Li-storage processes during long-term cycling.

It appeared that the unique morphology and structure of the $NiO/Ni_3V_2O_8$ NPAs after 100 cycles with charge were the key feature for the excellent electrochemical performance of the $NiO/Ni_3V_2O_8$ NPAs. It was discovered that the morphology of cycled $NiO/Ni_3V_2O_8$ NPAs was much different from the original morphology (Fig. 6a). The $NiO/Ni_3V_2O_8$ NPAs after 100 cycles had a new film-like porous structure which assembled with numbers of nanoparticles as seen from a high magnification SEM image of $NiO/Ni_3V_2O_8$ NPAs (Fig. 6b). TEM results (Fig. 6c) showed that the mean size of the most nanoparticle was around 10–30 nm, whereas the HRTEM image of cycled $NiO/Ni_3V_2O_8$ NPAs showed that the crystal lattice spacing was 0.238 nm corresponding to the (022) plane for NiO, which was consistent with the results of *ex situ* X-ray (Fig. 4c-f). Such microstructural evolution along with the cycling process could be ascribed to a very unique and novel reconstruction process.[49] It indicated that the initial size reduction of $NiO/Ni_3V_2O_8$ NPAs produced numbers of nanoparticles, and the reassembly of these nanoparticles formed a secondary structure during cycling process. The newly formed film-like porous architecture might facilitate improve the reaction kinetics of the $NiO/Ni_3V_2O_8$ NPAs, which was responsible for the outstanding lithium storage properties.

The EIS (100 kHz to 0.01 Hz, 5 mV s^{-1}) was employed to explore the origin of excellent electrochemical properties of $NiO/Ni_3V_2O_8$ NPAs with various states (Fig. 7). The fresh and cycled $NiO/Ni_3V_2O_8$ samples were fitted by equivalent circuit and the fitted results were summarized in Table S3.† Results revealed that R_s of the $NiO/Ni_3V_2O_8$ samples increased slightly

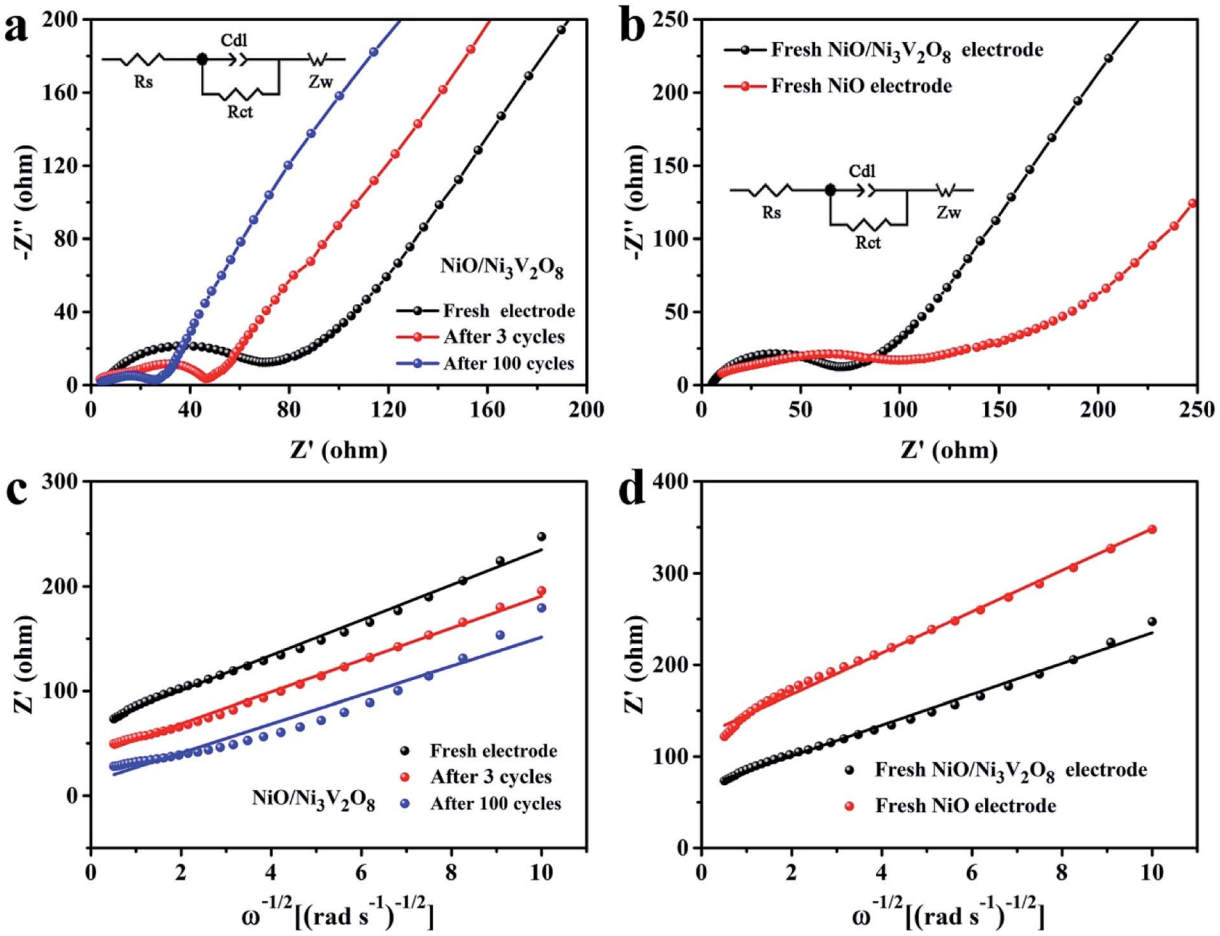

Fig. 7 EIS spectra of (a) the $NiO/Ni_3V_2O_8$ NPAs after different cycles and (b) fresh $NiO/Ni_3V_2O_8$ NPAs and bare NiO samples (the insert was the equivalent circuit, where R_s is the SEI film and/or contact resistance, R_{ct} is the charge-transfer impedance on samples/electrolyte interface, C_{dl} is the capacitance related to the double layer, and Z_w represents the lithium-diffusion process within samples). The relationship between the real parts Z' and $\omega^{-1/2}$ for (c) the $NiO/Ni_3V_2O_8$ NPAs after different cycles, (d) fresh $NiO/Ni_3V_2O_8$ NPAs and NiO samples.

as the formation of SEI films produced by the morphology change of $NiO/Ni_3V_2O_8$ NPAs in cycling. Meanwhile, R_{ct} decreased with the increase of cycle number, indicating the decrease of charge-transfer impedance, which might be associated with the novel electrochemical reconstruction as demonstrated in Fig. 6. The newly formed film-like porous architecture during the cycling process consisted of many small-sized $NiO/Ni_3V_2O_8$ nanoparticles, which facilitated the electric contact between $NiO/Ni_3V_2O_8$ NPAs and Ti foil, resulting in the enhanced electrochemical performance of the integrated $NiO/Ni_3V_2O_8$ NPAs. Fig. 6b showed that the fresh $NiO/Ni_3V_2O_8$ NPAs exhibited a lower R_s and R_{ct} than those of NiO samples. The reduction of resistance might derive from the presence of the $Ni_3V_2O_8$ crystals. Fig. 7(c and d) displayed the relationship between the real parts Z' of the impedance and $\omega^{-1/2}$ in the low frequency region, the Warburg factor σ could be calculated from the slope of the line Z'–$\omega^{-1/2}$ ($\sigma = Z'/\omega^{-1/2}$), which was inversely proportional to the diffusion coefficient of Li-ion.[52,53] That was to say, the smaller the value of σ was, the higher the diffusion coefficient of Li-ions showed. It was seen that the Warburg factor σ for the $NiO/Ni_3V_2O_8$ NPAs decreased slightly in value along with the cycling number (Fig. 7c, Table S3†), indicating enhanced Li-ion diffusion process. Both the reduced size and the favorable microstructural evolution in cycling might be responsible for the improved kinetics properties of the $NiO/Ni_3V_2O_8$ NPAs. Furthermore, the Warburg factor σ was 16.82 for the fresh $NiO/Ni_3V_2O_8$ NPAs and 22.59 for the fresh NiO electrode (Fig. 7d), suggesting that the kinetics property of $NiO/Ni_3V_2O_8$ NPAs was better than that of fresh NiO electrode, which was consistent with the charge/discharge results.

As is discussed above, the outstanding electrochemical properties of $NiO/Ni_3V_2O_8$ NPAs could be ascribed to several aspects. Firstly, the direct growth of hierarchical $NiO/Ni_3V_2O_8$ nanostructures on Ti foil could ensure robust mechanical adhesion and short transportation length for both Li^+ and electrons. Secondly, the $NiO/Ni_3V_2O_8$ NPAs constructed an open and highly porous framework structure, which facilitate the electrolyte penetration and Li^+ migration as well as the accommodation of strains during the cycling process. Thirdly, the novel electrochemical reconstruction of the $NiO/Ni_3V_2O_8$ NPAs during the cycling process could favor to improve kinetics properties of conversion and intercalation reaction, leading to enhanced electrochemical performances. Moreover, the synergistic effect between NiO and $Ni_3V_2O_8$ is not obviously neglectable, which can account for the superior performance of $NiO/Ni_3V_2O_8$ NPAs.

4 Conclusions

We had successfully prepared a hierarchical $NiO/Ni_3V_2O_8$ NPAs using a facile one-step hydrothermal method, followed by subsequent annealing treatment. The resultant $NiO/Ni_3V_2O_8$ NPAs took an open and highly porous framework structure, assembled by interpenetrated nanoplatelets with the thickness of about 60–80 nm, in which the NiO and $Ni_3V_2O_8$ subunits were homogeneously dispersed. Compared with the bare NiO electrode, the $NiO/Ni_3V_2O_8$ NPAs rendered high reversible capacity of 1169.3 mA h g^{-1} after 100 cycles at 200 mA g^{-1}, delivered 570.1 mA h g^{-1} after 600 cycles at 1000 mA g^{-1}, and retained 427.5 mA h g^{-1} even at 8000 mA g^{-1}. The superior lithium storage performance could be ascribed to the rationally designed composition and nanostructure of the $NiO/Ni_3V_2O_8$ NPAs. The possible mechanism of electrochemical reaction of $NiO/Ni_3V_2O_8$ NPAs would be the common conversion and intercalation reactions of nickel/vanadium based multiple oxides. These results suggested that $NiO/Ni_3V_2O_8$ NPAs can be used as advanced electrodes for next generation LIBs. This work may open a new avenue to design and synthesis hierarchical nanostructure with a synergistic effect.

Conflicts of interest

There are no conflicts to declare.

Acknowledgements

The work was supported by National Natural Science Foundation of China (No. 51502309), the Science and Technology Research Program of Chongqing Municipal Education Commission (Grant No. KJQN201801411) and the Science and Technology Project Program of Chongqing Fu-Ling district Science and Technology Commission (Grant No. FLKJ, 2018BBA3047).

References

1 N. S. Choi, Z. Chen, S. A. Freunberger, X. Ji, Y. K. Sun, K. Amine, G. Yushin, L. F. Nazar, J. Cho and P. G. Bruce, *Angew. Chem., Int. Ed.*, 2012, **51**, 9994–10024.
2 C. Masquelier and L. Croguennec, *Chem. Rev.*, 2013, **113**, 6552–6591.
3 M. M. Thackeray, C. Wolverton and E. D. Isaacs, *Energy Environ. Sci.*, 2012, **5**, 7854.
4 S. Ni, J. Liu, D. Chao and L. Mai, *Adv. Energy Mater.*, 2019, **9**, 1803324.
5 N. Mahmood, T. Tang and Y. Hou, *Adv. Energy Mater.*, 2016, **6**, 1600374.
6 W. Qi, J. G. Shapter, Q. Wu, T. Yin, G. Gao and D. Cui, *J. Mater. Chem. A*, 2017, **5**, 19521–19540.
7 W. Zhang, X. Xiao, Y. Zhang, J. Li, J. Zhong, M. Li, X. Fan, C. Wang and L. Chen, *Nanotechnology*, 2018, **29**, 105705.
8 A. Huang, Y. He, Y. Zhou, Y. Zhou, Y. Yang, J. Zhang, L. Luo, Q. Mao, D. Hou and J. Yang, *J. Mater. Sci.*, 2018, **54**, 949–973.
9 X. Sun, C. Yan, Y. Chen, W. Si, J. Deng, S. Oswald, L. Liu and O. G. Schmidt, *Adv. Energy Mater.*, 2014, **4**, 1300912.
10 X. Sun, W. Si, X. Liu, J. Deng, L. Xi, L. Liu, C. Yan and O. G. Schmidt, *Nano Energy*, 2014, **9**, 168–175.
11 B. Jiang, C. Han, B. Li, Y. He and Z. Lin, *ACS Nano*, 2016, **10**, 2728–2735.
12 X. Xiong, C. Yang, G. Wang, Y. Lin, X. Ou, J. H. Wang, B. Zhao, M. Liu, Z. Lin and K. Huang, *Energy Environ. Sci.*, 2017, **10**, 1757–1763.
13 X. Gao, J. Wang, D. Zhang, K. Nie, Y. Ma, J. Zhong and X. Sun, *J. Mater. Chem. A*, 2017, **5**, 5007–5012.

14 H. Pang, B. Guan, W. Sun and Y. Wang, *Electrochim. Acta*, 2016, **213**, 351–357.
15 A. A. AbdelHamid, Y. Yu, J. Yang and J. Y. Ying, *Adv. Mater.*, 2017, **29**, 1701427.
16 J. Zhang, W. Luo, T. Xiong, R. Yu, P. Wu, J. Zhu, Y. Dai and L. Mai, *Nanoscale*, 2019, **11**, 7588–7594.
17 S. Shen, W. Guo, D. Xie, Y. Wang, S. Deng, Y. Zhong, X. Wang, X. Xia and J. Tu, *J. Mater. Chem. A*, 2018, **6**, 20195–20204.
18 C. a. Zhou, X. Xia, Y. Wang, Y. Zhong, Z. Yao, X. Wang and J. Tu, *J. Mater. Chem. A*, 2017, **5**, 1394–1399.
19 S. Deng, Y. Zhang, D. Xie, L. Yang, G. Wang, X. Zheng, J. Zhu, X. Wang, Y. Yu, G. Pan, X. Xia and J. Tu, *Nano Energy*, 2019, **58**, 355–364.
20 Q. Xie, Y. Zhu, P. Zhao, Y. Zhang and S. Wu, *J. Mater. Sci.*, 2018, **53**, 9206–9216.
21 J. Li, Z. Li, F. Ning, L. Zhou, R. Zhang, M. Shao and M. Wei, *ACS Omega*, 2018, **3**, 1675–1683.
22 X. Xie, T. Makaryan, M. Zhao, K. L. Van Aken, Y. Gogotsi and G. Wang, *Adv. Energy Mater.*, 2016, **6**, 1502161.
23 J. G. Wang, D. Jin, R. Zhou, C. Shen, K. Xie and B. Wei, *J. Power Sources*, 2016, **306**, 100–106.
24 Y. Sharma, N. Sharma, G. V. Subba Rao and B. V. R. Chowdari, *Adv. Funct. Mater.*, 2007, **17**, 2855–2861.
25 C. Yuan, H. B. Wu, Y. Xie and X. W. Lou, *Angew. Chem., Int. Ed.*, 2014, **53**, 1488–1504.
26 A. Jain, B. J. Paul, S. Kim, V. K. Jain, J. Kim and A. K. Rai, *J. Alloys Compd.*, 2019, **772**, 72–79.
27 J. Huang, W. Wang, X. Lin, C. Gu and J. Liu, *J. Power Sources*, 2018, **378**, 677–684.
28 J. S. Park, J. S. Cho and Y. C. Kang, *J. Power Sources*, 2018, **379**, 278–287.
29 X. Liu, J. Wang and G. Yang, *ACS Appl. Mater. Interfaces*, 2018, **10**, 20688–20695.
30 L. Niu, Y. Wang, F. Ruan, C. Shen, S. Shan, M. Xu, Z. Sun, C. Li, X. Liu and Y. Gong, *J. Mater. Chem. A*, 2016, **4**, 5669–5677.
31 S. Lu, T. Zhu, Z. Li, Y. Pang, L. Shi, S. Ding and G. Gao, *J. Mater. Chem. A*, 2018, **6**, 7005–7013.
32 C. Lv, J. Sun, G. Chen, C. Yan and D. Chen, *Nano Energy*, 2017, **33**, 138–145.
33 C. Zhou, S. Fan, M. Hu, J. Lu, J. Li, Z. H. Huang, F. Kang and R. Lv, *J. Mater. Chem. A*, 2017, **5**, 15517–15524.
34 Y. Yang, Y. Liu, K. Pu, X. Chen, H. Tian, M. Gao, M. Zhu and H. Pan, *Adv. Funct. Mater.*, 2017, **27**, 1605011.
35 J. Yu, S. Chen, W. Hao and S. Zhang, *ACS Nano*, 2016, **10**, 2500–2508.
36 J. Q. Li, Y. H. Sun, M. X. Huang and J. M. Nan, *J. Alloys Compd.*, 2019, **788**, 690–700.
37 T. Li, X. Li, Z. Wang, H. Guo, Q. Hu and W. Peng, *Electrochim. Acta*, 2016, **191**, 392–400.
38 J. Xu, L. He, Y. Wang, C. Zhang and Y. Zhang, *Electrochim. Acta*, 2016, **191**, 417–425.
39 X. Xu, K. Cao, Y. Wang and L. Jiao, *J. Mater. Chem. A*, 2016, **4**, 6042–6047.
40 Y. Lu, L. Yu, M. Wu, Y. Wang and X. W. D. Lou, *Adv. Mater.*, 2018, **30**, 1702875.
41 Y. Zhang, Q. Zhuo, X. Lv, Y. Ma, J. Zhong and X. Sun, *Electrochim. Acta*, 2015, **178**, 590–596.
42 L. Qiao, X. Wang, L. Qiao, X. Sun, X. Li, Y. Zheng and D. He, *Nanoscale*, 2013, **5**, 3037–3042.
43 Z. Wang, S. Zhang, H. Zeng, H. Zhao, W. Sun, M. Jiang, C. Feng, J. Liu, T. Zhou, Y. Zheng and Z. Guo, *ChemPlusChem*, 2018, **83**, 915–923.
44 P. Vishnukumar, B. Saravanakumar, G. Ravi, V. Ganesh, R. K. Guduru and R. Yuvakkumar, *Mater. Lett.*, 2018, **219**, 114–118.
45 G. Yang, H. Cui, G. Yang and C. Wang, *ACS Nano*, 2014, **8**, 4474–4487.
46 B. Sambandam, V. Soundharrajan, V. Mathew, J. Song, S. Kim, J. Jo, D. P. Tung, S. Kim and J. Kim, *J. Mater. Chem. A*, 2016, **4**, 14605–14613.
47 R. Dedryvère, S. Laruelle, S. Grugeon, P. Poizot, D. Gonbeau and J. M. Tarascon, *Chem. Mater.*, 2004, **16**, 1056–1061.
48 S. Laruelle, S. Grugeon, P. Poizot, M. Dollé, L. Dupont and J. M. Tarascon, *J. Electrochem. Soc.*, 2002, **149**, A627.
49 S. Ni, B. Zheng, J. Liu, D. Chao, X. Yang, Z. Shen and J. Zhao, *J. Mater. Chem. A*, 2018, **6**, 18821–18826.
50 Q. Q. Xiong, J. P. Tu, X. H. Xia, X. Y. Zhao, C. D. Gu and X. L. Wang, *Nanoscale*, 2013, **5**, 7906–7912.
51 W. Guo, W. Sun and Y. Wang, *ACS Nano*, 2015, **9**, 11462–11471.
52 L. Zeng, F. Xiao, J. Wang, S. Gao, X. Ding and M. Wei, *J. Mater. Chem.*, 2012, **22**, 14284.
53 S. Ni, J. Zhang, J. Ma, X. Yang, L. Zhang, X. Li and H. Zeng, *Adv. Mater. Interfaces*, 2016, **3**, 1500340.